Clays and Clay Minerals, Vol. 55, No. 5, 453–466, 2007.

POLYTYPE AND MORPHOLOGICAL ANALYSES OF GÜMBELITE, A FIBROUS Mg-RICH ILLITE

JUN KAMEDA[1,*], RITSURO MIYAWAKI[2], VICTOR A. DRITS[3] AND TOSHIHIRO KOGURE[1]

[1] Department of Earth and Planetary Science, Graduate School of Science, The University of Tokyo, 7-3-1 Hongo, Bunkyo-ku, Tokyo, 113-0033, Japan
[2] Department of Geology, The National Science Museum, 3-23-1 Hyakunin-cho, Shinjuku-ku, Tokyo 169-0073, Japan
[3] Geological Institute, Russian Academy of Science, Pyzhevsky per. D7, 1109017 Moscow, Russia

Abstract—Polytypism in gümbelite and its relationship to the fibrous or ribbon-like morphology exhibited by this Mg-rich illite were investigated by powder X-ray diffraction (XRD), electron back-scattered diffraction (EBSD) and transmission electron microscopy (TEM). Comparison between the XRD pattern from oriented fibers using a conventional powder diffractometer and a randomly oriented pattern using a Gandolfi camera suggested that $2M_2$ is dominant but other polytypes belonging to subfamily A also exist, and that the fiber axis of gümbelite is parallel to <110> in $2M_2$, <110> in $2M_1$, and <100> in $1M$. The EBSD analyses confirmed these crystallographic directions directly from individual crystals. Electron diffraction and high-resolution TEM showed that twinning and intergrowths of various polytypes including both subfamilies are common in a single crystal and that the two types of rotations [$2n60^\circ$ and $(2n+1)60^\circ$] between adjacent layers are often randomly mixed at the monolayer level. The data suggest that high densities of twinning and intergrowths account for the origin of the fibrous morphology along <110> for $2M_1$ and $2M_2$ polytypes. Volume restriction in a confined vein space may also play a role.

Key Words—EBSD, HRTEM, Illite, Morphology, Polytype, Stacking Disorder.

INTRODUCTION

Polytypism is a common phenomenon observed in many kinds of phyllosilicates. In the case of the mica group, polytypes are generated by rotation between adjacent layers, the angle of which is restricted to $n60^\circ$ ($0 \leqslant n \leqslant 5$) about the [001]* direction. Although the number of polytypes in micas is theoretically infinite, polytypes in which the position of any layer relative to the others is the same or equivalent for all layers (MDO polytypes, Ďurovič, 1992) are specific and limited to only six; they are designated as $1M$, $2M_1$, $2M_2$, $2O$, $3T$ and $6H$ using the notation of Ramsdell (1947). These six polytypes can be further divided into two subfamilies, A and B (Nespolo and Ďurovič, 2002). In subfamily A ($1M$, $2M_1$, $3T$), the rotation angle is 0° or $\pm120^\circ$ (n is even), which results in an offset of octahedral sheets along the same direction for every layer. In subfamily B ($2O$, $2M_2$, $6H$), on the other hand, the rotation angle is 180° or $\pm60^\circ$ (n is odd), and the octahedral offsets alternate in orientation along the stacking direction.

Mica polytypes in subfamily B occur far less commonly than those in subfamily A. This can be attributed to the different atomic arrangements in the interlayer regions of the subfamilies. In subfamily B, the basal oxygen atoms in the tetrahedral sheets on opposite sides of the interlayer cations are exactly superimposed along the [001]* direction. In subfamily A, the superposed basal oxygen atoms are laterally displaced from each other owing to the ditrigonal distortion of the tetrahedral rings. Nevertheless, polytypes in subfamily B ($2M_2$ and $2O$) have been reported in several natural mica specimens. Lepidolite, a Li-bearing mica with Al as the dominant octahedral cation, is known to adopt the $2M_2$ polytype frequently (*e.g.* Levinson, 1953). The $2O$ polytype was first reported in anandite, a mica with Ba as the interlayer cation and S substituting for OH (Giuseppetti and Tadini, 1972). Recently, the $2O$ polytype was observed for phlogopite (Kogure and Nespolpo, 1999; Ferraris *et al.*, 2001).

Illite, an interlayer-deficient dioctahedral mica with Al as the dominant octahedral cation, occasionally has been reported to bear subfamily B polytypes. The $2M_2$ polytype in illite (hydromuscovite in the original literature) was first reported by Threadgold (1959). Although the powder XRD pattern from $2M_2$ illite resembles that of a mixture of $1M$ and $2M_1$ polytypes (Radoslovich, 1960), the existence of $2M_2$ illite was confirmed by Shimoda (1970). The crystal structure of $2M_2$ illite was refined by using electron diffraction (Zhoukhlistov *et al.*, 1973). The existence of the $2O$ polytype was suggested in hydrothermal illite by a microtopographic study using atomic force microscopy (Kuwahara *et al.*, 2001). The conditions that favor polytypes in subfamily B have been discussed by several researchers (Radoslovich, 1958; Abbott and Burnham, 1988; Ni and Hughes, 1996; Brigatti *et al.*, 2005).

* E-mail address of corresponding author:
kameda@eps.s.u-tokyo.ac.jp
DOI: 10.1346/CCMN.2007.0550501

However, no conclusive explanation for the occurrence of subfamily B polytypes has been made, especially for illite.

Gümbelite was described for the first time by Dana (1892) as a mineral close to pyrophyllite, with the crystal having a flexible ribbon-like form. Mg-rich illite is now recommended usage in preference to gümbelite (Riedel *et al.*, 1999), in light of its crystal structure and chemical composition. However, we use 'gümbelite' in the present study to denote an illite variety specimen with a distinct morphology and polytype. Aruja (1944) examined gümbelite by XRD and reported that it has a unit-cell with a = 5.21, b = 9.02, c = 20.12 Å and β = 96.0º. These parameters are very similar to those of muscovite. He also suggested that the gümbelite crystals are predominantly elongated along the [110] direction. Drits *et al.* (1966) analyzed gümbelite by using X-ray and oblique texture electron diffraction, and found that the sample was a mixture of $2M_2$ (predominant) and $2M_1$ polytypes. They used a non-standard $2M_2$ unit-cell with a = 5.20, b = 9.00, c = 20.4 Å and α = 100.0º, and they found that the elongation of the fibers coincides with the <110> direction in both modifications.

In the present paper, we describe details of the stacking structure in gümbelite as revealed by XRD, EBSD and TEM. We particularly focus on the polytypes that characterize gümbelite and the relationship between crystal morphology and crystallographic orientation.

SAMPLE AND METHODS

The gümbelite specimen originated from Shunga, Zaonezhye peninsula, Lake Onega, Karelia, Russia. The geological occurrence of the gümbelite was described by Timofeev (1937) and Tokmakov *et al.* (1961). Gümbelite occurs as vein-filling fibrous crystals in Carboniferous slates with its fiber axis perpendicular to the vein wall, but it often protrudes in lens-like shapes along the foliation of the shale. These veins are 1−2 cm thick and several meters long, and are filled with virtually pure gümbelite. Figure 1 shows an SEM image of the specimen. The crystals with ribbon-like morphology often assemble to form bundles.

Chemical analysis of our gümbelite sample by wet methods showed that it consists of 49.35% SiO_2; 0.66% TiO_2; 29.20% Al_2O_3; 0.86% Fe_2O_3; 4.14% MgO; 0.30% CaO and 8.80% K_2O. These data are almost identical to the chemical analysis of a gümbelite sample from a Karelian shungite, determined by Timofeev and given by Aruja (1944). A structural formula calculated for 22 negative charges is

$$K_{0.75}Ca_{0.02}(Al_{1.62}Ti_{0.03}Fe^{3+}_{0.04}Mg_{0.41})_{2.10}(Si_{3.31}Al_{0.69})O_{10}(OH)_2$$

Illite is characterized by a small interlayer cation concentration and a significant fraction of octahedral Mg. The sum of the octahedral cations is slightly higher than that expected for a pure dioctahedral 2:1 layer, probably indicating the existence of small trioctahedral clusters within the dioctahedral matrix of the 2:1 layer. Although it is generally accepted that *trans*-octahedra ($M1$ sites) are vacant in dioctahedral phyllosilicates, a detailed structural determination of $2M_1$ phengites and $2M_1$ muscovites showed that a small excess of electron density exists in some of the $M1$ sites (Güven, 1971; Brigatti *et al.*, 1998).

The specimen was crushed gently and placed in the dimple of a glass sample holder. X-ray diffraction patterns were collected using a conventional powder diffractometer (Rigaku RINT-Ultima+) with graphite-monochromated CuKα radiation. The XRD analysis using a Gandolfi camera of 114.6 mm in diameter employing Ni-filtered CuKα radiation was also conducted for a specimen several hundreds of micrometers long, attached to a thin glass fiber. The patterns were recorded with an imaging plate and processed with a Fuji BAS-2500 bio-imaging analyzer and with a program developed by Nakamuta (1999).

For EBSD analyses, the gümbelite specimen was suspended in deionized water and dispersed on a silicon wafer coated with a Pt-Pd film. The sample then was coated with a thin carbon film. The Pt-Pd film on the silicon wafer was used for acquiring the background intensity subtracted from EBSD patterns for the specimen. The EBSD analyses were carried out using an Hitachi S-4500 SEM with a cold field-emission gun and a ThermoNoran PhaseID system. The acceleration voltage and specimen current were 20 kV and 2−3 nA, respectively, for the acquisition of EBSD patterns. The acquisition time was normally ~10 s. During the acquisition, the electron beam was rastered over an area of ~3 μm × 3 μm on the specimen to reduce radiation damage by the intense electron current (Kogure *et al.*, 2005). Drawing Kikuchi patterns and

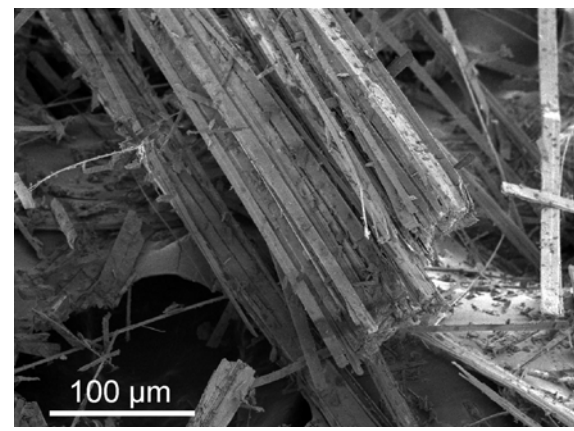

Figure 1. SEM image of the gümbelite crystallites showing a fibrous or ribbon-like morphology. The gümbelite crystallites that are several hundred micrometers long often assemble to form large bundles.

analyses of the acquired EBSD patterns were performed using a program developed by Kogure (2003).

Specimens for TEM observation were prepared by using a method similar to that described by Kogure (2002a). The specimen was embedded in epoxy resin between two glass slides. After hardening, the glass slides were cut using a diamond wheel to laths of ~1 mm thick. The laths were thinned to ~50 μm by mechanical grinding and finished by argon ion milling. Examination by HRTEM was performed at 200 kV using a JEOL JEM-2010 TEM with a nominal point resolution of 0.2 nm (C_s = 0.5 mm). Degradation of gümbelite by electron radiation was so rapid that generally only one exposure was possible to obtain HRTEM images. Some successful images recorded on film were digitized using a CCD camera for image processing. Noisy contrast from amorphous materials on the specimen surface was removed using a background subtraction filtering technique (Kilaas, 1998) implemented with Gatan Digital Micrograph version 2.5. Chemical compositions were determined locally by an energy-dispersive X-ray (EDX) detector mounted on the TEM and a Kevex Sigma spectrum analyzer.

RESULTS

XRD analysis of gümbelite

Figure 2a,b shows XRD patterns from 15 to 40º2θ obtained with the Gandolfi camera and conventional diffractometer, respectively. Figure 2c–e (broken lines) represents calculated diffraction patterns for the three polytypes: $2M_2$ (c), $2M_1$ (d) and $1M$ (e). In these calculations, atomic coordinates reported by Zhoukhlistov *et al.* (1973), Mookherjee *et al.* (2001) and Sidorenko *et al.* (1975) were used for $2M_2$, $2M_1$ and $1M$, respectively. It is expected that the pattern obtained with the Gandolfi camera reflects highly randomized orientations, as is ideal for polytype analysis. It is apparent that the $2M_2$ polytype structure accounts for nearly all of the diffraction features observed in Figure 2a, but the two peaks indicated with an asterisk can be assigned only to a $2M_1$ polytype, suggesting that the specimen does not consist of a single polytype. The cell parameters for the $2M_2$ polytype determined from nine distinct peaks in the XRD pattern are a = 9.03(2), b = 5.21 (1), c = 20.26 (2) Å and β = 100.1 (1)º. The values of these parameters suggest that the *trans*-octahedra of the 2:1 layers are vacant (Bailey, 1984). Indeed, $c\cos\beta/a = -0.393$, suggesting that the intralayer shift (the lateral shift from the lower tetrahedral sheet to the upper tetrahedral sheet within the 2:1 layer) for each individual 2:1 layer is $-0.393a_u$ along the a_u axis of the unit layer with $a_u < b_u$, assuming that the lateral cell dimension of the unit layer is a_u = 5.21, b_u = 9.03 Å and γ_u = 90º (the subscript 'u' indicates the cell parameters for the unit layer). This value is typical for the *trans*-vacant $1M$ illite because the apical oxygen atoms of the opposing tetrahedral sheets in a 2:1 layer are linked to elongated unshared diagonal octahedral edges (Bailey, 1984). From these values, the cell parameters for the $2M_1$ polytype are estimated to be a = 5.21, b = 9.03, c = 20.05 Å and β = 95.8º. Table 1 represents the experimental d values for the distinct peaks in Figure 2a and the calculated values using these proposed cell parameters, showing a good agreement between them.

The pattern obtained with the conventional diffractometer (Figure 2b) is considerably different from that using the Gandolfi camera (Figure 2a). First, the 00l basal reflections are considerably stronger. This preferred orientation is common to many phyllosilicates with a well developed basal plane. Second, several strong peaks distinctive in Figure 2a are missing or relatively weakened in Figure 2b. This is explained as follows: because gümbelite has a fibrous morphology as seen in the SEM image (Figure 1), the crystals tend to be oriented with their fiber axis parallel to the specimen holder. Hence, reflections from the lattice planes that are parallel to the fiber axis of the crystal are enhanced. Drits *et al.* (1966) reported that the crystallographic direction of the fiber axis is <110> in the $2M_2$ polytype. Figure 2c shows the calculated pattern (the solid line) consisting of reflections indexed only with hhl and $h\bar{h}l$. These peaks are clearly stronger in the diffraction pattern of the specimen with preferred orientation (Figure 2b) relative to that of the sample with random orientation (Figure 2a), supporting the idea that the fiber direction is parallel to <110>.

It is also evident that the two peaks with an asterisk for the $2M_1$ polytype in Figure 2a are nearly absent in Figure 2b. As described below, EBSD analysis showed that the $2M_1$ crystals are elongated along <110> as well. These peaks are indexed to the (023) and the (025) planes in the $2M_1$ polytype, and they are expected to be weakened in the pattern of the oriented specimen if the elongation is parallel to <110> of the $2M_1$ polytype. On the contrary, the peak indicated with the arrowhead is distinct in Figure 2b, although it is weak in Figure 2a. This peak can be assigned to neither $2M_1$ nor $2M_2$, but to 023 in the $1M$ polytype (or 109 in $3T$). If these $1M$ crystals are elongated along <100>, as was reported by Güven *et al.* (1980) and as is shown in the EBSD analysis later, this peak should be enhanced in the oriented specimen.

Identification of polytype and determination of crystallographic orientation by EBSD

As described by Kogure (2002b) and Kogure and Bunno (2004), Kikuchi bands for phyllosilicates are divided into three categories: (1) hkl with $h = 3n$ and $k = 3n$; (2) hkl with $h \neq 3n$ and $k = 3n$; and (3) others with $k \neq 3n$ if the indices are expressed using the orthohexagonal C-centered cell (note that the h and k indices are exchanged for the $2M_2$ polytype because the a and b axes are exchanged). Kikuchi bands in the first category are

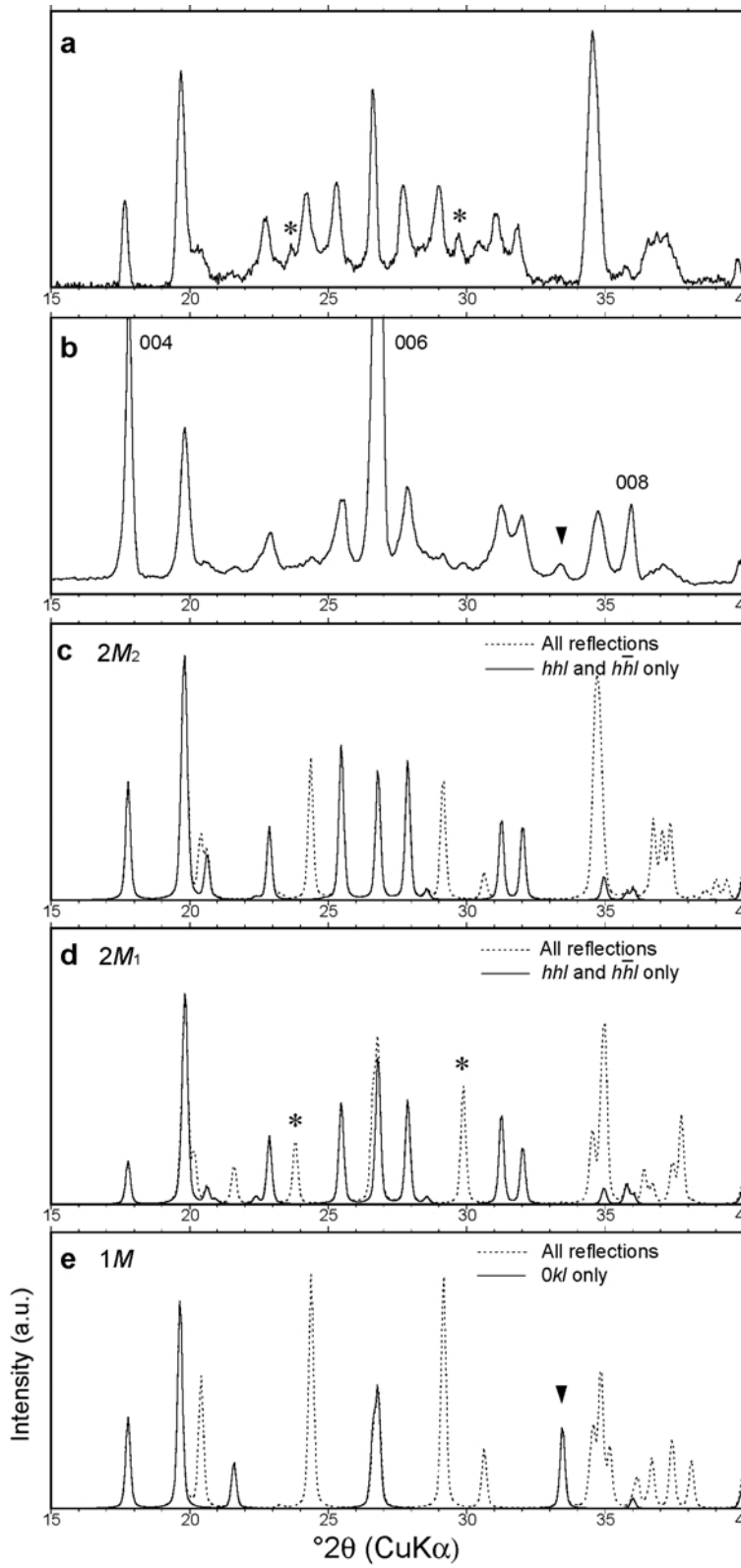

Figure 2. (a, b) XRD patterns from gümbelite obtained using a Gandolfi camera (a) and a conventional diffractometer (b). (c–e) Calculated XRD patterns for the $2M_2$ (c), $2M_1$ (d) and $1M$ (e) polytypes. Asterisks and arrowheads in the figure indicate the characteristic peaks for $2M_1$ and $1M$, respectively. Broken and solid lines represent the calculated patterns from all reflections and specific reflections, respectively.

Table 1. Experimental and calculated d values for $2M_2$ and $2M_1$ polytypes.

$I_{obs.}$	$d_{obs.}$ (Å)	$2M_2$ $d_{calc.}$* (Å)	$2M_2$ hkl	$2M_1$ $d_{calc.}$** (Å)	$2M_1$ hkl
100	9.98	9.97	002	9.97	$\bar{0}02$
32	5.00	4.99	004	4.99	004
81	4.48	4.49	110	4.49	110
		4.47	$\bar{1}11$	4.47	$\bar{1}11$
19	3.88	3.89	$\bar{1}13$	3.89	$\bar{1}13$
6	3.73			3.73	023
25	3.65	3.65	$\bar{2}04$		
28	3.50	3.50	$\bar{1}14$	3.50	$\bar{1}14$
69	3.33	3.32	006	3.32	006
28	3.20	3.20	114	3.20	114
25	3.07	3.06	204		
10	2.99			2.99	025
4	2.91	2.92	$\bar{2}06$		
15	2.86	2.86	115	2.86	115
15	2.80	2.79	$\bar{1}16$	2.79	$\bar{1}16$
94	2.59	2.59	$\bar{3}12$	2.59	200
		2.58	021		
6	2.49	2.49	008	2.49	008
19	2.42	2.40	312	2.40	$\bar{2}04$
9	2.26	2.25	$\bar{4}02$	2.26	040
				2.26	$\bar{2}21$
7	2.08	2.07	$\bar{3}17$	2.07	223
28	2.00	1.99	00*10*	1.99	00*10*
25	1.51	1.50	$\bar{6}02$	1.51	20*10*
		1.50	$\bar{3}31$		
9	1.30	1.30	$\bar{6}23$	1.30	$\bar{4}02$
		1.30	041	1.30	260
				1.30	$\bar{2}62$
				1.30	400

* Calculated from cell parameters: a = 9.03, b = 5.21, c = 20.26 Å, β = 100.1°
** Calculated from cell parameters: a = 5.21, b = 9.03, c = 20.05 Å, β = 95.8°

common to all polytypes. Those in the second category are common to polytypes in the same subfamily, and those in the third category are characteristic of each polytype. Kogure and Bunno (2004) discriminated the 1*M*, $2M_1$ and $2M_2$ polytype in lepidolite in the following way. At first, subfamilies A and B were distinguished by the pseudo-trigonal and pseudo-hexagonal symmetries, respectively, formed by the bands in the second category. Then each polytype was identified by the bands described by the third category. Kogure and Bunno (2004) reported that several characteristic Kikuchi bands, such as $\bar{1}12$, $1\bar{1}2$ and 022 in 1*M*, and 114, $\bar{1}\bar{1}4$ and 025 in $2M_1$, and 114, $1\bar{1}4$, 204 and $\bar{2}04$ in $2M_2$, are sufficiently intense to be used for identification of these polytypes. The same procedure was applied to the present sample.

Figure 3 shows SEM images of gümbelite crystals, EBSD patterns acquired from the crystals, calculated Kikuchi patterns and stereographic projections of the crystallographic axes. The EBSD patterns show hexagonal symmetry around [001]*, suggesting that the crystals belong to subfamily B. These patterns also exhibit relatively sharp Kikuchi bands indexed to the (114), (204) and $(1\bar{1}4)$ planes, which belong to the third category and nearly coincide with the calculated $2M_2$ patterns (Figure 3e,f). On the other hand, Figure 4 shows EBSD patterns with trigonal symmetry around [001]*, suggesting that the crystals belong to subfamily A. By further trial to find the best fit to the experimental patterns, it was found that patterns in Figures 4c and 4d correspond to the $2M_1$ and 1*M* polytypes, respectively. These analyses confirm our XRD results that the gümbelite specimen contains a mixture of polytypes. Although only a few EBSD patterns were clear enough for polytype identification (probably due to the high intergrowth density of several polytypes, as shown later in the TEM analysis), and statistical analysis is difficult, the patterns of the $2M_2$ polytype were more common than those of the polytypes belonging to subfamily A.

Figures 3 and 4 also show the directions of the crystallographic axes of the crystals determined by analyses of the EBSD patterns in the form of stereographic projections. By comparing these projections with the SEM images, it is shown that both the $2M_2$ and $2M_1$ polytypes are elongate in a direction almost parallel to <110>, whereas the 1*M* polytype is elongate in the

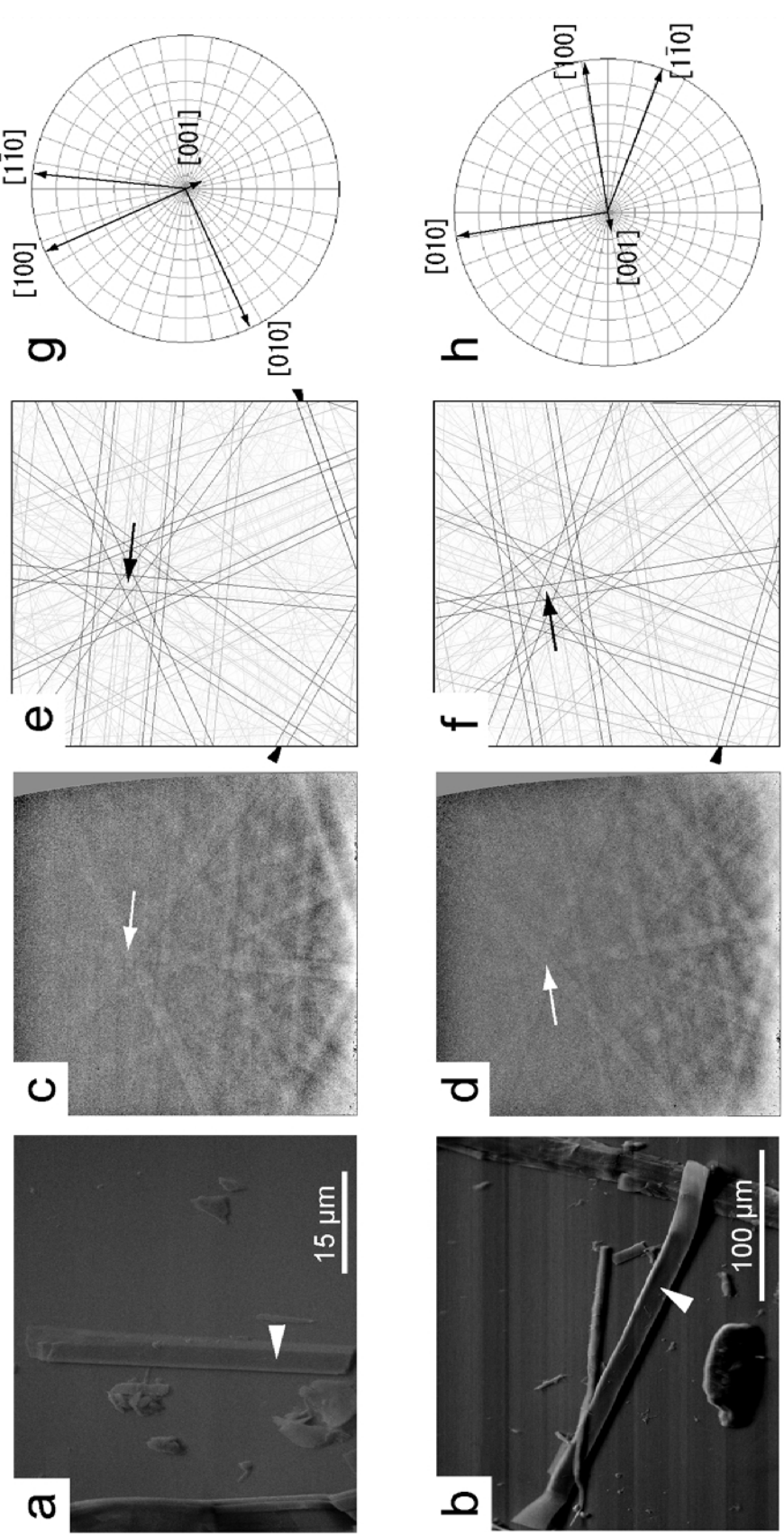

Figure 3. (a, b) SEM images of the crystals analyzed. EBSD patterns were acquired from the points marked by white arrows. (c, d) Acquired EBSD patterns and (e, f) corresponding Kikuchi patterns calculated by crystal parameters for the $2M_2$ polytype. Hexagonal symmetry along the [001]* direction is indicated by white (c,d) and black (e, f) arrows. Several Kikuchi bands, characteristic of the $2M_2$ polytype, are also shown with their indices in (e, f). (g, h) Stereographic projections showing the orientations of the crystallographic axes.

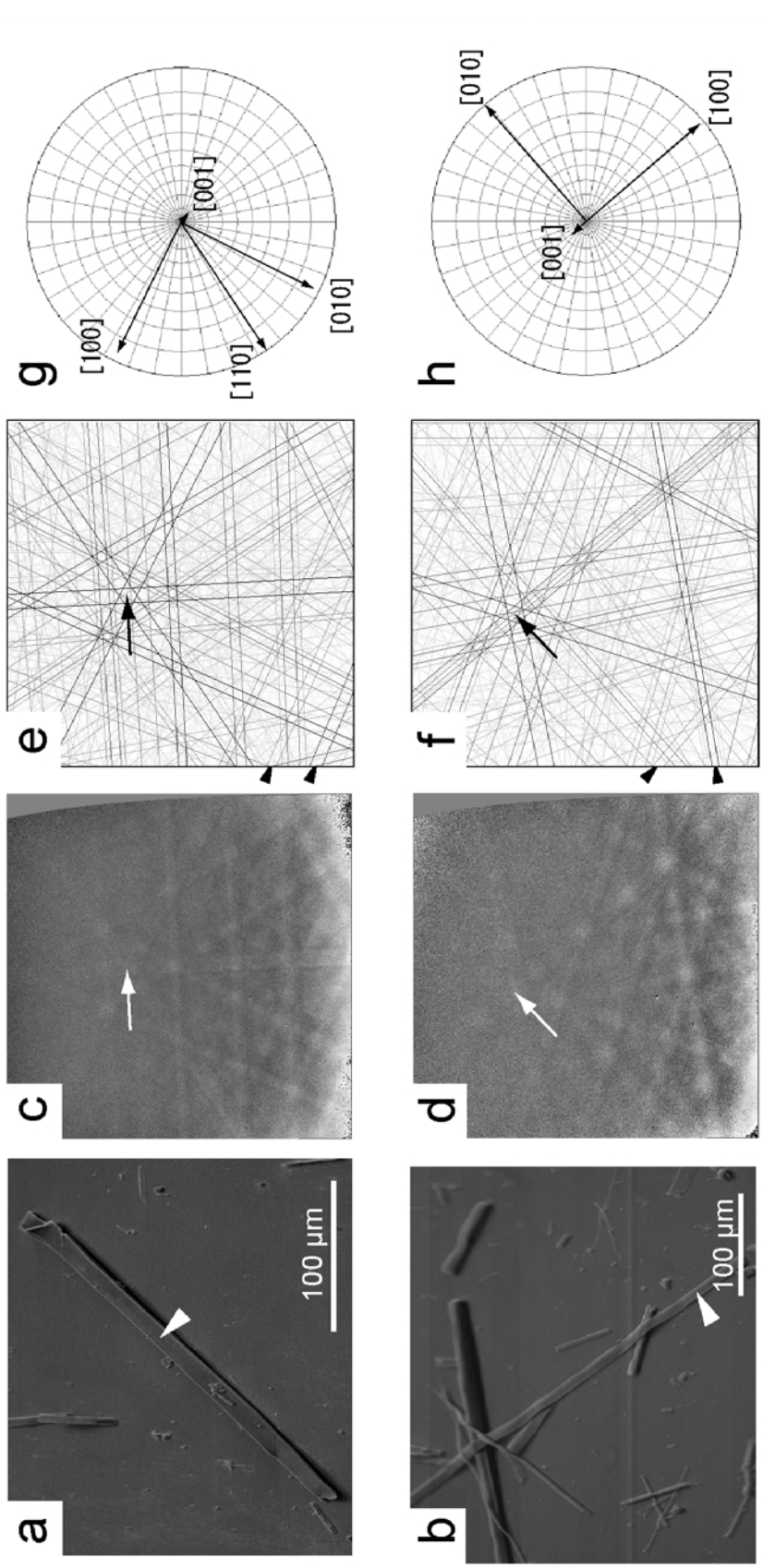

Figure 4. (a, b) SEM images of the crystals analyzed. EBSD patterns were acquired from the area marked by white arrows. (c, d) EBSD patterns and corresponding Kikuchi patterns calculated by crystal parameters for the $2M_1$ (e) and $1M$ (f) polytypes. The trigonal symmetry along the [001]* direction is indicated by white (c, d) and black (e, f) arrows. Several identified Kikuchi bands characteristic of $2M_1$ and $1M$ are also shown with their indices in (e, f). (g, h) Stereographic projections showing the directions of the crystallographic axes.

[100] direction. These results are consistent with the XRD analyses, as discussed above. Drits *et al.* (1966) hypothesized that the ribbons of gümbelite consist of small $2M_2$ domains elongated along the *a* axis (they used the *a* and *b* axes with $a < b$) and offset by ±60º from the fiber axis to pack into a hexagonal parquet. However, if a gümbelite crystal is actually composed of such small fragments, the Kikuchi bands with $k \neq 3n$ are expected to become obscure in EBSD patterns because the technique averages information within the rastered area of ~3 μm × 3 μm. Our EBSD patterns contain the distinctive Kikuchi bands with $k \neq 3n$ (Figure 3), indicating that the rastered area comprises not small fragments but a single crystal.

HRTEM observation of gümbelite

Because TEM images of our specimen reveal intergrowths of different polytypic sequences, we express the principal crystallographic directions with 'X_i' and 'Y_i' in this section. X_i represents the crystallographic axes for the pseudohexagonal network and Y_i represents the directions rotated from adjacent X_i directions by 30º about the [001]* direction (Bailey, 1984). For instance, X_i corresponds to ±[010], ±[$\bar{1}\bar{1}$0] and ±[1$\bar{1}$0] (±[*uvw*] represents [*uvw*] and [$\bar{u}\bar{v}\bar{w}$]), and Y_i corresponds to ±[100], ±[$\bar{1}$30] and ±[$\bar{1}\bar{3}$0] in $2M_2$. Figure 5 shows several types of selected-area electron diffraction patterns along Y_i. In Figure 5a, a two-layer periodicity is distinct in the left lattice row (the appearance of 00*l* reflections with *l* = odd number is attributed to dynamical diffraction). The appearance of the two-layer periodicity in the diffraction pattern along Y_i is characteristic of all polytypes in subfamily B (in the case of subfamily A, a one-layer periodicity appears along Y_i (Bailey, 1988)). However, careful examination shows that the pattern does not form an orthogonal lattice (notice that the spot in the left lattice row is not on the white line drawn horizontally from the center spot). This deviation from orthogonality cannot occur in the 2*O* and 6*H* polytypes, and it must represent a zone axis belonging to the Y_i family of the $2M_2$ polytype except ±[100] which is parallel to the glide plane, with the intralayer shift in a unit layer deviating from $-a_u/3$ ($-0.393a_u$ as described above).

Figure 5b represents a pattern similar to that in Figure 5a, but each spot in the left row is split into a pair. This SAED pattern also arises from the $2M_2$ polytype, but the diffraction region consists of domains with different orientations, probably formed by rotational twinning. Figure 5c is an enlargement of a portion of the pattern in Figure 5b. One interpretation is that the spots indicated by the white arrows are from domains with the beam direction along [130] (the same as the pattern in Figure 5a) and the spots with the black arrows are domains with beam direction along [$\bar{1}$30] or [$\bar{1}\bar{3}$0]. Such a rotational twinning results from stacking disorder involving a regular alternation of +60º and −60º rotations in the $2M_2$ stacking sequence.

The diffraction pattern in Figure 5d is also generated by our specimen. This pattern is interpreted as a mixture of subfamilies A and B. Figure 5e shows the dark field image formed with the diffraction spots in the circle in

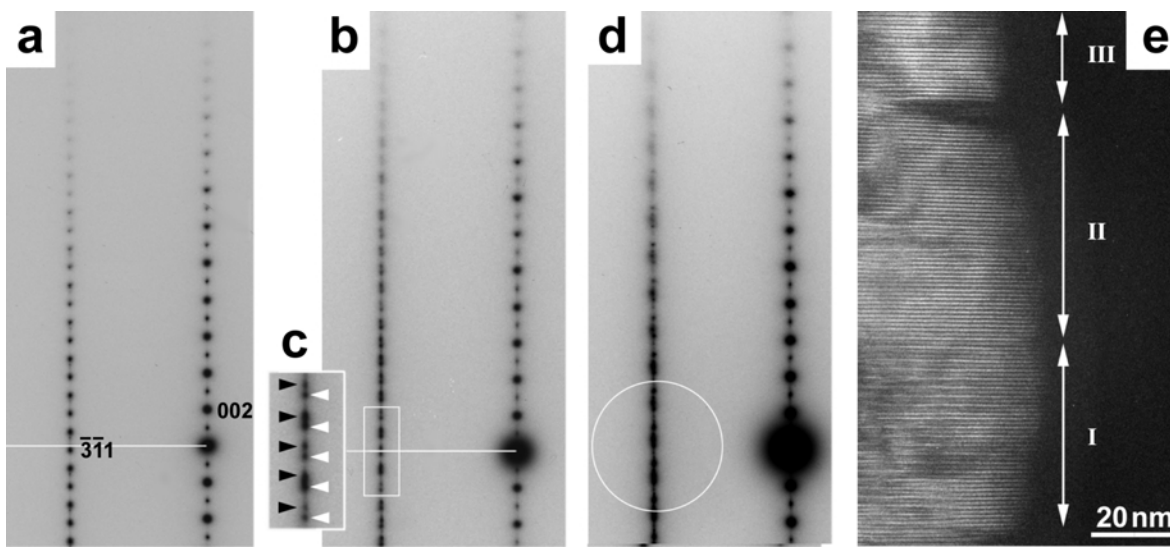

Figure 5. (a) Selected area diffraction pattern from a nearly ordered region, showing two-layer periodicity along the reciprocal lattice row on the left. The polytype is identified as $2M_2$ viewed along [1$\bar{3}$0] (see the text). (b) Pattern with split spots in the left row probably due to rotational twins about the [001]* axis in the $2M_2$ polytype. (c) Enlarged pattern of the region bounded by the white rectangle in (b) (see the text). (d) Pattern with more complex spots and streaking. (e) Dark field image using diffraction spots within the white circle in (d). The region indicated with 'I' shows a two-layer (2.0 nm) periodicity but the region with 'II' has a one-layer periodicity. The region marked 'III' is disordered.

Figure 5d. The lattice fringes in the region indicated with 'I' exhibit a two-layer periodicity, whereas these in region II have a one-layer periodicity. Lattice fringes in region III are heavily disordered. This result suggests that the stacking sequences in the two subfamilies can be mixed in gümbelite. This is confirmed by the HRTEM image along the Y_i direction in Figure 6 (see Kogure, 2002a, for the interpretation of the contrast in the image). The white bar in the right of Figure 6b connects the closest dark spots that correspond to individual tetrahedra between the lower and upper tetrahedral sheets in a 2:1 layer. The sign (+ or −) at each 2:1 layer indicates the direction of the slant of the white bar. These signs must alternate in subfamily B whereas they are uniform in subfamily A (Kogure, 2002a). Actually they are neither uniform nor alternate, proving that the two types of the stacking sequences can be mixed at a monolayer level. This is consistent with our previous result for lepidolite (Kogure and Bunno, 2004).

Several HRTEM images along the X_i direction are shown in Figure 7. As described by Kogure (2002a), unambiguous determination of polytypes in micas is impossible from HRTEM imaging along only one direction but a second image of the same region along another direction constrains the identification. However, gümbelite is readily damaged by an intense electron beam, and HRTEM imaging along two zone axes is not feasible. Therefore, multiple candidates for 'maximum degree of order' (MDO) polytypes as determined from the contrast variations observed within regions having ordered stacking sequences are indicated in the figure. For instance, the contrast at the upper left part of Figure 7, which has one-layer periodicity and oblique dark bars in each 2:1 layer, can be assigned to 1*M* viewed along [110] or [$\bar{1}$10], or $2M_2$ viewed along [0$\bar{1}$0]. Similarly two candidate MDO polytypes can be derived from the contrast in the other areas depicted in Figure 7. An exception is the image at the bottom-right, which has a three-layer periodicity, such that 3*T* is the only allowable MDO polytype. Although it is possible to ascribe some areas to the 2*O* polytype, as shown in the figure, probably this polytype is rare, considering the results from other analyses as described above.

Finally the relationship between specific polytypic sequences and compositional variations was investigated by using TEM-EDX analysis at regions with ordered stacking. However, a significant difference in the compositions among the polytypes was not detected

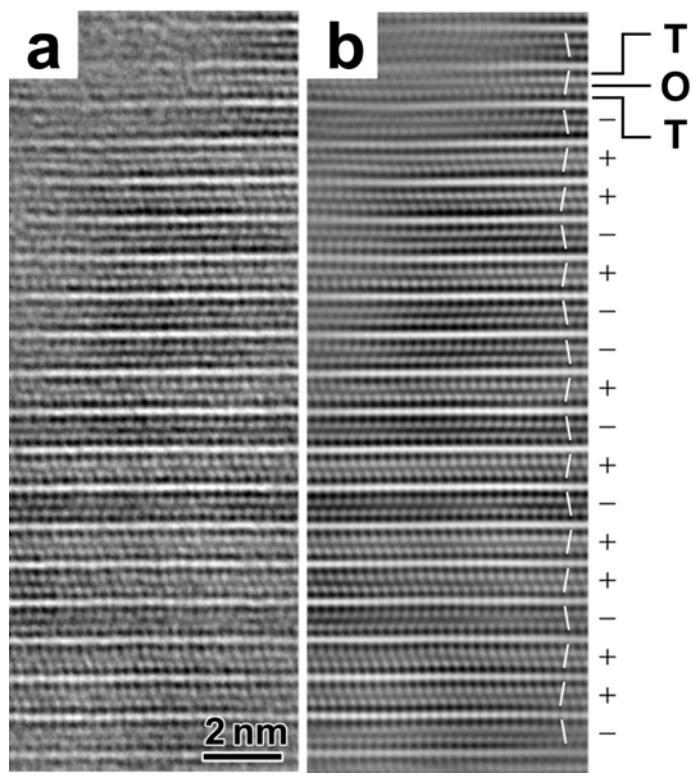

Figure 6. (a) Original and (b) filtered HRTEM images of a disordered region, recorded along the Y_i direction. T and O to the right of (b) indicate tetrahedral sheet and octahedral sheet, respectively. The white bars connect the closest dark spots, which correspond to individual tetrahedra, between the lower and upper tetrahedral sheets in a 2:1 layer. The sign (+ or −) at each 2:1 layer indicates the direction of the slant of the white bar. These signs must alternate for subfamily B, whereas they are uniform for subfamily A. They are disordered in the figure, suggesting mixed stacking of subfamilies A and B.

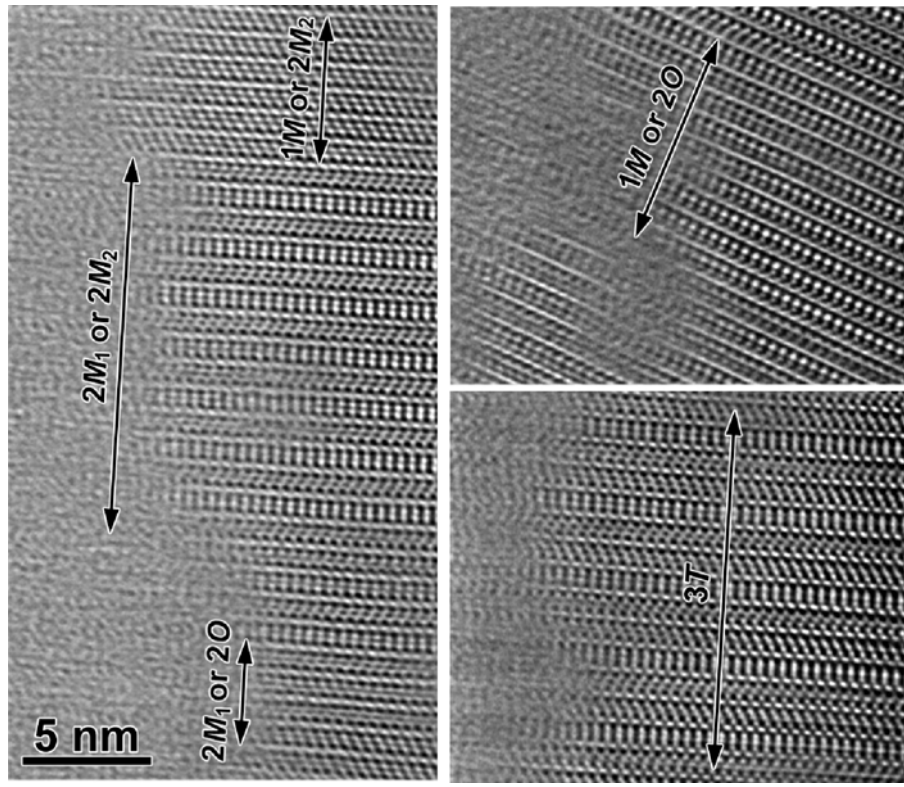

Figure 7. Filtered HRTEM images recorded along the X_i direction. Possible MDO polytypes derived from the HRTEM contrast are indicated in the figures (see the text for detail).

within the experimental variance (the specimen is beam-sensitive and the variance is large owing to the limited electron dose to avoid element diffusion).

DISCUSSION

Mutual orientation of the successive 2:1 layers in the $2M_2$ and $2M_1$ illites with respect to their crystallographic elongation

In order to understand our analyses of polytypism in gümbelite, the crystallographic relationships between mica polytypes are reviewed briefly here. The orientation of each 2:1 layer in the $2M_1$ and $2M_2$ polytypes can be characterized by the direction of its a_u axis, located in the layer mirror plane. The origin of the layer unit-cell is chosen in the center of the ditrigonal ring of the lower tetrahedral sheet of the layer. For simplicity one can assume that in 2:1 layers of both polytypes, the center of the ditrigonal ring of the upper tetrahedral sheet in projection on the (001) plane is shifted with respect to that of the lower tetrahedral sheet along the a_u axis by $a_u/3$, and that the centers of the ditrigonal rings of the tetrahedral sheets forming an interlayer cavity and belonging to adjacent 2:1 layers coincide in the projection on the (001) plane. Let us assume that the a_u axis of the lowest 2:1 layer in the $2M_2$ polytype is parallel to the vertical in Figure 8a and is oriented downward, as shown by arrow 1. In projection on the (001) plane, the dashed lines join the centers of the ditrigonal rings of the lower (point A) and upper (B) tetrahedral sheets of the layer. The next layer can be rotated counter-clockwise by 60º with respect to the first one

As mentioned above, the centers of the ditrigonal rings of the lower tetrahedral sheet of the upper layer and the upper tetrahedral sheet of the lower layer coincide (point B). The dashed line rotated with respect to the first line clockwise by 60º about B connects the centers of the lower tetrahedral sheet (B) and the upper tetrahedral sheet (C) in the rotated next layer and arrow 2 shows its orientation. The dashed line between points A and C joins the centers of the ditrigonal rings of the lower tetrahedral sheets and other equivalent structural points of the nearest 2:1 layers having identical orientation. Because in the $2M_2$ illite structure the a_u axes of the odd and even 2:1 layers are parallel to those of layer 1 and layer 2, respectively, then the *a* and *b* axes of the $2M_2$ unit-cell should be oriented as shown in Figure 8a. Note that the selection of the *a* and *b* axes are exchanged compared with that for the 1*M* and $2M_1$ polytypes because the axis perpendicular to the symmetry (*c* glide) plane should be set as the *b* axis in the monoclinic system. As can be seen in the figure, the $[1\bar{1}0]$ direction of the $2M_2$ unit-cell is parallel to the a_u axis of the odd layers. Comparison of Figures 8a and 3

shows that if the experimental and calculated orientations of the *a* and *b* axes of the $2M_2$ unit-cell are compared, then the a_u axis of the odd layers coincides with the elongation of the $2M_2$ crystals.

Similarly, Figure 8b shows a case when one layer is rotated with respect to an adjacent one clockwise by 120º, leading to the $2M_1$ structure. The [110] direction of the $2M_1$ unit-cell is parallel to the a_u axis of the odd layers, and if the experimental and calculated orientations of the *a* and *b* axes of the $2M_1$ unit-cell are compared, then the a_u axis of the odd layers coincides with the elongation of the $2M_1$ crystals (compare Figures 8b and 4a). Thus in the fibrous $2M_2$ and $2M_1$ crystals, the odd (or even) layers are oriented with the a_u axes parallel to the direction of crystal elongation. Moreover, orientation of the *a* axis in the $2M_2$ crystals coincides with that of the *b* axis in the $2M_1$ crystals whereas the corresponding *b* and *a* axes of these crystals have the opposite orientation (Figure 8a,b). Therefore, a coexistence of thin $2M_1$ and $2M_2$ layer packets can be formed by rotation of some even layers by 180º with respect to each other. In 1*M* crystals, laths are parallel to the a_u- (= $a-$) axes of all stacking layers.

Possible origin of the fibrous shape of the $2M_2$ and $2M_1$ illite crystals

The origin of the fibrous morphology of illite has been discussed for several decades (*e.g.* Wilson and Pittmann, 1977; Bauer *et al.*, 2000; Güven, 2001). Several experimental studies have been performed to synthesize illite in order to elucidate the kinetic conditions favorable to its fibrous growth (Güven *et al.*, 1982; Small *et al.*, 1992; Bauer *et al.*, 2000). These studies along with observations of illite particle morphology during illite diagenesis in sandstones (Lanson and Champion, 1991; Lanson *et al.*, 1996) suggested that the lath shape is a transient phenomenon and eventually transforms to platy illite. Small *et al.* (1992) performed a precipitation experiment of illite at 250ºC containing oxalate and suggested that very rapid precipitation resulted in the fibrous/lath morphology. Bauer *et al.* (2000), on the other hand, pointed out that at lower temperature conditions (~100ºC) a slow growth rate and lower supersaturation conditions favor the occurrence of fibrous illite.

In addition to these kinetic effects, the relationship between the polytypic features and morphology of illite also has been discussed. In general, a crystal habit is determined by the difference in growth rates among individual crystallographic directions. It was reported that lath-shaped crystals are typical for 1*M* illite elongated along the *a* axis (*e.g.* Güven *et al.*, 1980). This morphological feature may be related to an inhibitory effect by inorganic or organic complexes on the (010) facet during crystal growth (Güven, 2001). In contrast, the $2M_1$ illite polytype tends to form a diamond or pseudo-hexagonal morphology (*e.g.* Inoue *et al.*, 1987; Baronnet, 1992). Al-rich $2M_2$ illite described by Slonimskaya *et al.* (1978) also has a platy morphology (data not shown). The $2M_1$ and $2M_2$ polytypes must intrinsically have the same growth rate along [110] and [1$\bar{1}$0], because they are crystallographically equivalent. Hence if these crystals grow in a free space (*e.g.* in solution) and via homogeneous nucleation, it is not expected that the crystal will elongate along only one of these two equivalent directions. Thus, the fibrous morphology of $2M_2$ and $2M_1$ gümbelite crystals elongated along one of the <110> is quite mysterious.

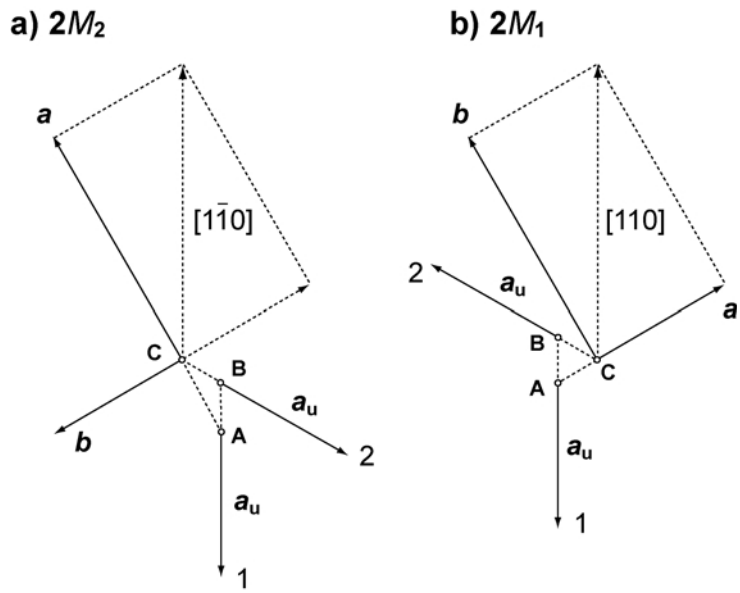

Figure 8. Relationship between the orientation of the successive 2:1 layers in the $2M_2$ (a) and $2M_1$ (b) polytypes and their crystallographic axes (see the text).

Although the two <110> directions in $2M_2$ and $2M_1$ are crystallographically equivalent, the two directions can be differentiated if a crystal has intergrowths of different polytypes or twinning. As described above, twins and/or intergrowths of different polytypes in a crystal are very common in the present specimen. Such a stacking disorder can change the populations of the unit layers with their a_u axis along the [110] and [1$\bar{1}$0] directions, which are equal in the ordered two-layer polytypes. For instance, if domains of $2M_2$ and $2M_1$ coexist in almost equal ratios in a crystal, then the layers whose a_u axis is shared by both polytypes (*e.g.* layer 1 in Figure 8) are twice as abundant as those with the other orientations (layer 2 in Figure 8a,b). According to studies of fibrous 1*M* illite (Güven *et al.*, 1980), it is possible that the growth rate of the illite unit layer is very fast along the a_u axis, or very slow along the b_u axis. Hence the crystal can elongate along the direction to which the unit layers whose a_u axes are parallel are most abundant.

Based on their TEM observations, Tokmakov *et al.* (1961) argued that gümbelite fibers are preferentially oriented in the main body of the vein whereas relatively randomly oriented fibers were recognized in the vicinity of the boundary to the Shungite shale. From this occurrence, Tokmakov *et al.* (1961) suggested that a geometrical selection mechanism caused the fibrous morphology of gümbelite. If a nucleation density on the wall is very high, a growth competition between adjacent crystals may occur and lead to a fibrous morphology of growing minerals (*e.g.* Cox, 1987). The nucleation of randomly oriented crystals within the narrow confines at the vein wall generates small, equant crystals. Those crystals oriented with their fast growth directions normal to the vein wall will out-compete other crystals, resulting in fiber development. This geometrical selection rule may promote the growth of the fiber axis of gümbelite with one of the <110> directions because of the intrinsically faster growth rate than those along other crystallographic directions as described above.

Factors promoting the formation of $2M_2$ polytypes

Occurrences of specific polytypes of mica have often been correlated with compositional variations. For example, Abbot and Burnham (1988) showed by energy calculations that the value indicating the degree of corrugation of basal oxygen surface (Δz) is the best parameter for prediction of polytypes. They noted that values of $\Delta z < 0.01$ correspond to the 1*M* polytype whereas higher values favor the $2M_1$ polytype. Δz decreases with increasing substitution of (Mg, Fe) because the sizes of the *M*1 and *M*2 octahedra become closer (Lee and Guggenheim, 1981; Brigatti *et al.*, 1998). In fact, Peacor *et al.* (2002) showed by TEM-AEM analyses that unusually high Mg contents in illite sequences are associated with the 1*M* polytype, which can be attributed to lower Δz values.

Recently Drits *et al.* (2006) carried out an analysis of the relationship between $(2n + 1)60°$ rotational stacking faults and cation composition of the 2:1 layers for a large collection of illite-smectites (I-S) and illites. They showed that the amount of these stacking faults depends mostly on the total Al content in the octahedral and tetrahedral sheets of the 2:1 layers. They argued that smaller Al contents cause the decrease in both tetrahedral rotation and Δz values. Even when $Al_{tot} \approx 2.2$ atoms per $O_{10}(OH)_2$, the concentration of $(2n + 1)60°$ stacking faults (P_{60}) may be equal to 40% of the total amount of rotational defects (Drits *et al.*, 2006). The coexistence of $2M_2$, $2M_1$ and 1*M* illite polytypes in the present sample as well as within individual crystals with stacking faults due to rotation of the layers by $2n60°$ and/or $(2n + 1)60°$ may be considered as evidence for the absence of rigid restrictions on the mutual arrangements of the layers, which is probably caused by lower tetrahedral rotation and Δz. Nevertheless, it is evident that the $2M_2$ polytype, or ±60° rotations, is dominant in the present sample. Why high Mg contents and correspondingly low Al content cause the abundance of the $2M_2$ polytype instead of the 1*M* polytype as predicted by Abbot and Burnham (1988) is uncertain at present.

It is, however, interesting that this result is very similar to the result for the occurrence of the $2M_2$ polytype in lepidolite. The composition of lepidolite is represented as a ternary system consisting of polylithionite ($KLi_2AlSi_4O_{10}F_2$), trilithionite [$KLi_{3/2}Al_{3/2}Si_3AlO_{10}(OH,F)_2$] and muscovite [$KAl_2Si_3AlO_{10}(OH)_2$]. Munoz (1968) reported that the $2M_2$ polytype, as well as the 1*M* and 3*T* polytypes, only appear in compositions that contain considerable amounts (close to half or more) of polylithionite. This implies that $2M_2$ lepidolite may appear with a small Al content, although it is also possible to speculate that a large Li or F content is responsible for $2M_2$ (Levinson, 1953; Takeda *et al.*, 1971). The relationship between the Al content and polytype occurrence in lepidolite was also reported by Kogure and Bunno (2004). This similarity between lepidolite and illite strongly suggests that a small Al content is responsible for the $2M_2$ polytype, or ±60° rotations.

Drits *et al.* (2006) reported that P_{60} is inversely correlated with the total Al content (Al_{tot}), which is the summation of Al in the tetrahedral sheets (Al_{tetr}) and octahedral sheet (Al_{oct}). Because Al_{tetr} and Al_{oct} in their samples are approximately correlated, probably due to the Tschermak substitution ($^{VI}Mg^{IV}Si \rightleftharpoons {}^{VI}Al^{IV}Al$), these contents are not independent. It seems that Al content in the tetrahedral sheet (Al_{tetr}) is more responsible for the preference of ±60° rotations because it contributes directly to the atomic arrangement around the interlayer region. X-ray structure analyses determine only average atomic positions of the tetrahedral sheet with randomly distributed Al at the tetrahedral sites, but

it is likely that the local atomic positions are considerably modulated by the Al substitution. The interlayer cavities are formed with twelve tetrahedra in the lower and upper tetrahedral sheets. In case of the ideal muscovite composition [$KAl_2Si_3AlO_{10}(OH)_2$], three Al tetrahedra participate to construct one cavity. On the other hand, this is close to two in the present gümbelite sample. We cannot answer at present, for instance, why two (or fewer) Al tetrahedra seem to promote ±60º rotations. Hopefully future works using computer simulations may yield the solution.

ACKNOWLEDGMENTS

We are grateful to T. Takeshige (of the University of Tokyo) for preparation of the TEM specimens. Electron microscopy was performed in the Electron Microbeam Analysis Facility of Department of Earth and Planetary Science, the University of Tokyo. This work was partly supported by a Grant-in-Aid No. 17340160 (Section (B)) from the Japan Society for the Promotion of Science (JSPS).

REFERENCES

Abbott, R.N. Jr. and Burnham, C.W. (1988) Polytypism in micas: A polyhedral approach to energy calculations. *American Mineralogist*, **73**, 105–118.

Aruja, E. (1944) An X-ray study on the crystal-structure of gümbelite. *Mineralogical Magazine*, **27**, 11–16.

Bailey, S.W. (1984) Crystal chemistry of the true micas. Pp. 13–60 in: *Micas* (S.W. Bailey, editor). Reviews in Mineralogy, **13**, Mineralogical Society of America, Washington, D.C.

Bailey, S.W. (1988) X-ray diffraction identification of the polytypes of mica, serpentine, and chlorite. *Clays and Clay Minerals*, **36**, 193–213.

Baronnet, A. (1992) Polytypism and stacking disorder. Pp. 231–288 in: *Minerals and Reactions at the Atomic Scale: Transmission Electron Microscopy* (R.P. Buseck, editor). Reviews in Mineralogy, **27**, Mineralogical Society of America, Washington, D.C.

Bauer, A., Velde, B. and Gaupp, R. (2000) Experimental constraints on illite crystal morphology. *Clay Minerals*, **35**, 587–597.

Brigatti, M.F., Frigieri, P. and Poppi, L. (1998) Crystal chemistry of Mg-, Fe-bearing muscovites-2M_1. *American Mineralogist*, **83**, 775–785.

Brigatti, M.F., Caprilli, E., Malferrari, D., Medici, L. and Poppi, L. (2005) Crystal structure and chemistry of trilithionite-2M_2 and polylithionite-2M_2. *European Journal of Mineralogy*, **17**, 475–481.

Cox, S.F. (1987) Antitaxial crack-seal vein microstructures and their relationship to displacement paths. *Journal of Structural Geology*, **7**, 779–787.

Dana, J.D. (1892) *Descriptive Mineralogy*, 6th edition. J. Wiley and Sons, New York.

Drits, V.A., Zvyagin, B.B. and Tokmakov, P.P. (1966) Gümbelite – dioctahedral micas 2M_2. *Doklady Academii Nauk SSSR*, **170**, 1390–1394.

Drits, V.A., McCarty, D.K. and Zviagina, B.B. (2006) Crystal-chemical factors responsible for the distribution of octahedral cations over *trans*- and *cis*-sites in dioctahedral 2:1 layer silicates. *Clays and Clay Minerals*, **54**, 131–152.

Ďurovič, S. (1992) Layer stacking in general polytypic structures. Pp. 667–680 in: *International Tables for Crystallography Vol. C* (A.C.J. Wilson, editor). Kluwer Academic Publishers, Dordrecht, The Netherlands.

Ferraris, G., Gula, A., Ivaldi, G., Nespolo, M., Sokolova, E., Uvarova, Y. and Khomyakov, A.P. (2001) First structure determination of an MDO-2*O* mica polytype associated with a 1*M* polytype. *European Journal of Mineralogy*, **13**, 1013–1023.

Giuseppetti, G. and Tadini, C. (1972) The crystal structure of 2*O* brittle mica: anandite. *Tschermasks Mineralosische und Petrographische Mitteilungen*, **18**, 169–184.

Güven, N. (1971) The crystal structures of 2M_1 phengite and 2M_1 muscovite. *Zeitschrift für Kristallographie*, **134**, 196–262.

Güven, N. (2001) Mica structure and fibrous growth of illite. *Clays and Clay Minerals*, **49**, 189–196.

Güven, N., Hower, W.F. and Davies, D.K. (1980) Nature of authigenic illites in sandstone reservoirs. *Journal of Sedimentary Petrology*, **50**, 761–766.

Güven, N., Lafon, G.M. and Lee, L.J. (1982) Experimental hydrothermal alteration of albite to clays: preliminary results. *Proceedings of the International Clay Conference 1981*. Elsevier Scientific Publishing Company, pp. 495–512.

Inoue, A., Kohyama, N., Kitagawa, R. and Watanabe, T. (1987) Chemical and morphological evidence for the conversion of smectite to illite. *Clays and Clay Minerals*, **35**, 111–120.

Kilaas, R. (1998) Optical and near-optical filters in high-resolution electron microscopy. *Journal of Microscopy*, **190**, 45–51.

Kogure, T. (2002a) Investigation of micas using advanced TEM. Pp. 281–312 in: *Micas: Crystal Chemistry & Metamorphic Petrology* (A. Mottana, F.P. Sassi, J.B. Tompson, Jr. and S. Guggenheim, editors). Reviews in Mineralogy and Geochemistry, **46**, Mineralogical Society of America, and the Geochemical Society, Washington D.C.

Kogure, T. (2002b) Identification of polytypic groups in hydrous phyllosilicates using Electron Back-Scattering Patterns (EBSPs). *American Mineralogist*, **87**, 1678–1685.

Kogure, T. (2003) A program to assist Kikuchi pattern analysis. *Journal of the Crystallographic Society of Japan*, **45**, 391–395 (in Japanese with English abstract, the program was available from http:/www-gbs.eps.s.u-tokyo.ac.jp/kogure/edana).

Kogure, T. and Bunno, M. (2004) Investigation of polytype in lepidolite using electron back-scattered diffraction. *American Mineralogist*, **89**, 1680–1684.

Kogure, T. and Nespolo, M. (1999) First occurrence of a stacking sequence including (±60º, ±180º) rotations in Mg-rich annite. *Clays and Clay Minerals*, **47**, 784–792.

Kogure, T., Inoue, A. and Beaufort, D. (2005) Polytype and morphology analysis of kaolin minerals by Electron Back-Scattered Diffraction. *Clays and Clay Minerals*, **53**, 199–208.

Kuwahara, Y., Uehara, S. and Aoki, Y. (2001) Atomic force microscopy study of hydrothermal illite in Izumiyama pottery stone from Arita, Saga Prefecture, Japan. *Clays and Clay Minerals*, **49**, 300–309.

Lanson, B. and Champion, D. (1991) The I/S to illite reaction in the late stage diagenesis. *American Journal of Science*, **291**, 473–506.

Lanson, B., Beaufort, D., Berger, G., Baradat, J. and Lacharpagne, J.C. (1996) Illitization of diagenetic kaolinite-to-dickite conversion series: late-stage diagenesis of the lower Permian Rotlingend Sandstone reservoir, offshore of the Netherlands. *Journal of Sedimentary Research*, **66**, 501–518.

Lee, J.H. and Guggenheim, S. (1981) Single crystal X-ray refinement of pyrophyllite-1*Tc*. *American Mineralogist*, **66**, 350–367.

Levinson, A.A. (1953) Studies in the mica groups; relationship between polymorphism and composition in the muscovite-lepidolite series. *American Mineralogist*, **38**, 88–107.

Mookherjee, M., Redfern S.A.T. and Zhang, M. (2001) Thermal response of structure and hydneutron diffraction and FTIR study. *European Journal of Mineralogy*, **13**, 545–555.

Munoz, J.L. (1968) Physical properties of synthetic lepidolites. *American Mineralogist*, **53**, 1490–1512.

Nakamuta, Y. (1999) Precise analysis of a very small mineral by an X-ray diffraction method. *Journal of Mineralogical Society of Japan*, **28**, 117–121 (in Japanese with English abstract).

Nespolo, M. and Ďurovič, S. (2002) Crystallographic basis of polytypism and twinning in micas. Pp. 155–279 in: *Micas: Crystal Chemistry & Metamorphic Petrology* (A. Mottana, F.P. Sassi, J.B. Tompson, Jr. and S. Guggenheim, editors). Reviews in Mineralogy and Geochemistry, **46**, Mineralogical Society of America, Washington D.C.

Ni, Y. and Hughes, J.M. (1996) The crystal structure of nanpingite $2M_2$, the Cs end-member of muscovite. *American Mineralogist*, **81**, 105–110.

Peacor, D.R., Bauluz, B., Dong, H., Tillick, D. and Yan, Y. (2002) Transmission and analytical electron microscopy evidence for high Mg contents of 1*M* illite: Absence of 1*M* polytypism in normal prograde diagenetic sequences of politic rocks. *Clays and Clay Minerals*, **50**, 757–765.

Radoslovich, E.W. (1958) Structural control of polymorphism in micas. *Nature*, **183**, 253.

Radoslovich, E.W. (1960) Hydromuscovite with the $2M_2$ structure-A criticism. *American Mineralogist*, **45**, 894–898.

Ramsdell, L.S. (1947) Studies on silicon carbide. *American Mineralogist*, **32**, 64–82.

Riedel, M., Cavazzini, G., D'yakonov, Yu.S., Frank-Kamenetskii, V.A., Gottardi, G., Guggenheim, S., Koval, P.V., Muller, G., Neiva, A.M.R., Radoslovich, E.W., Robert, J.L., Sassi, F.P., Takeda, H., Weiss, Z. and Wones, D.R. (1999) Nomenclature of the micas. *Mineralogical Magazine*, **63**, 267–279.

Shimoda, S. (1970) A hydromuscovite from the Shakanai Mine, Akita Prefecture, Japan. *Clays and Clay Minerals*, **18**, 269–274.

Sidorenko, O.V., Zvyagin, B.B. and Soboleva, S.V. (1975) Refinement of crystal-structure of dioctahedral mica 1*M*. *Kristallografiya*, **20**, 543.

Slominskaya, M., Drits, V.A., Finco, V. and Salyn, A. (1978) The nature of interlayer water in fine-dispersed muscovite. *Preamurie in Izvestiya Akademii Nauk SSSR*, *seriya geol*., **10**, 95–104.

Small, J.S., Hamilton, D.L. and Habesch, S. (1992) Experimental simulation of clay precipitation within reservoir sandstones. 2. Mechanism of illite formation and controls on morphology. *Journal of Sedimentary Petrology*, **62**, 520–529.

Takeda, H., Haga, N. and Sadanaga, R. (1971) Structural investigation of polymorphic transition between $2M_2$-, 1*M*-lepidolite and $2M_1$ muscovite. *Mineralogical Journal*, **6**, 203–215.

Threadgold, I.M. (1959) A hydromuscovite with the $2M_2$ structure, from Mount Lyell, Tasmania. *American Mineralogist*, **44**, 488–494.

Timofeev, V.M. (1937) The northern excursion, The Karelian ASSR. Pp. 55 in: *XVII International Geological Congress Guide-book*. Leningrad, Moscow.

Tokumakov, P.P., Zamurueva, M.G. and Petrov, V.P. (1961) On the nature of gumbelite. *Trudy Instituta geologii rudnykh mestorozhdeniy, petrografii, mineralogii i geokhimii Akademii Nauk SSSR,* **48**, 80–93.

Wilson, M.D. and Pittmann, E.D. (1977) Authigenic clays in sandstones: Recognition and influence on reservoir properties and paleoenvironmental analysis. *Journal of Sedimentary Petrology*, **47**, 3–31.

Zhoukhlistov, A.P., Zvyagin, B.B., Soboleva, S.V. and Fedotov, A.F. (1973) The crystal structure of the dioctahedral mica $2M_2$ determined by high voltage electron diffraction. *Clays and Clay Minerals*, **21**, 465–470.

(*Received 20 March 2006; revised 17 March 2007; Ms. 1155; A.E. Peter J. Heaney*)